Depth-resolved fiber photometry with a single tapered optical fiber implant

Filippo Pisano [ID][1,4]*, Marco Pisanello [ID][1,4], Suk Joon Lee[2], Jaeeon Lee[2], Emanuela Maglie[1,3],
Antonio Balena[1,3], Leonardo Sileo[1], Barbara Spagnolo [ID][1], Marco Bianco[1,3], Minsuk Hyun[2],
Massimo De Vittorio [ID][1,3,5]*, Bernardo L. Sabatini [ID][2,5]* and Ferruccio Pisanello [ID][1,5]*

Fiber photometry is increasingly utilized to monitor fluorescent sensors of neural activity in the brain. However, most implementations are based on flat-cleaved optical fibers that can only interface with shallow tissue volumes adjacent to the fiber. We exploit modal properties of tapered optical fibers (TFs) to enable light collection over an extent of up to 2 mm of tissue and multisite photometry along the taper. Using a single TF, we simultaneously observed distinct dopamine transients in dorsal and ventral striatum in freely moving mice performing a simple, operant conditioning task. Collection volumes from TFs can also be engineered in both shape and size by microstructuring the nonplanar surface of the taper, to optically target multiple sites not only in the deep brain but, in general, in any biological system or organ in which light collection is beneficial but challenging because of light scattering and absorption.

n vivo fluorescence detection enables recording and studying functional signals from genetically defined neural populations in deep brain regions of freely moving animals[1]. For example, fiber photometry is used to monitor neural activity from specific cell types by recording fluorescence variations over time[2–9]. These approaches spurred the development of technologies based on photonics and optoelectronic platforms[10], as well as methods to record activities of multiple subpopulations using spectral multiplexing[11–13]. Typically, fiber photometry protocols rely on flat-cleaved optical fibers (FFs) to stimulate and collect fluorescence[2–9,11–19].

However, the accessible recording depth with FFs is restricted to the vicinity of the fiber tip, owing to tissue scattering and absorption effects, which, combined with the probe's geometry, determine the fluorescence excitation and collection efficiency[20,21]. Simple geometrical considerations indicate that the amount of signal that a FF collects decreases steeply with distance from the fiber facet[21]. Additionally, reconfiguring the collection geometry to reach multiple regions is not possible, because changing the light collection field requires repositioning the fiber. Furthermore, the geometric profile of FFs substantially damages tissue and, in the brain, induces glial activation around the device even long after the implantation[22,23]. Nonetheless, FFs are widely employed to assess neural activity from deep brain regions[3,11–19].

Here, we present an approach to overcome these limitations: we exploit the modal properties of light propagation in TFs to structure light collection patterns on the large optically active area of the taper and to access deeper cells. In addition to being less invasive than FFs[22], TF probes have unique light collection features, including: (i) a uniform interface over up to 2 mm of tissue along the fiber axis, (ii) the ability to perform multisite collection along the taper by time-division multiplexing, and (iii) the ability to design arbitrary collection volumes by microstructuring the nonplanar surface of the fiber taper.

Below, we quantify the three-dimensional (3D) light collection fields of TFs, finding that TFs collect fluorescence uniformly across large regions, such as the cerebral cortex and striatum in mice. When combined with large-area light delivery[22,24], this results in higher signal collection from TFs than FFs for similar illumination power density at the active optical surface. This is because the larger-area TFs can deliver more total illumination power, i.e., more photons, while exposing cells to a moderate power density. We show that, by exploiting site-selective light delivery and collection, TFs enable multipoint probing of functional fluorescence signals in freely moving animals, including dynamically recording signals from multiple brain regions along the fiber taper. We demonstrate the feasibility of such experiments by using a single TF in freely moving mice performing a reward-collection task and by quickly scanning the excitation light and simultaneously monitoring dopamine transients in dorsal and ventral striatum.

Finally, we combine modal effects governing light propagation along the taper with micro- and nanostructuring of the surface of metal-coated TFs to engineer the collection volume[25,26]. We restrict the collection volume to an angular portion of the taper surface, such that optical windows located at specific depths along the TFs interface with few cell bodies. Coupled with site-selective light delivery from optical windows[25], this approach provides a bidirectional interface with cellular volumes at depth with high spatial selectivity.

Results

Light collection properties of TFs. We characterized the light collection properties of TFs in a quasi-transparent fluorescent solution (Fig. 1). We implemented a two-photon scanning system to generate confined fluorescence spots, acting like isotropic point-like sources, in a PBS-fluorescein (30 μM) droplet in which we submerged the TFs (Fig. 1b). The fluorescence generated while raster scanning the spot around the taper was collected by two photomultiplier tubes
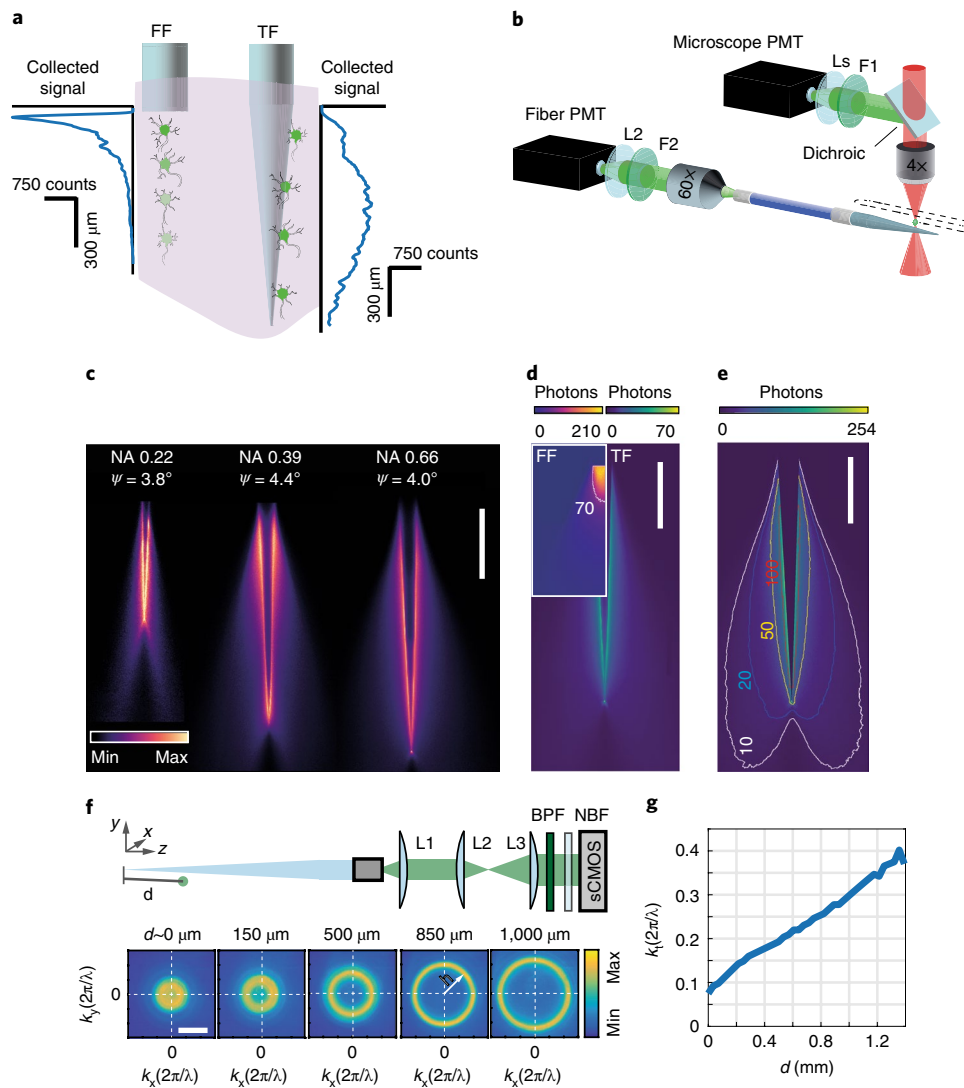
Fig. 1 | Light collection from TFs. a, Schematic of light collection from FF and TF in brain tissue. Experimental collection profiles are next to the fibers. **b**, Optical setup for imaging the light collection field of TFs. A two-photon excitation spot is scanned around a TF in a PBS-fluorescein droplet. The resulting fluorescence is detected by a non-descanned PMT (microscope PMT) and by the fiber PMT at the distal end of a patch fiber. Ls, lens system; F1 and F2, band-pass fluorescence filters; L2, lens. **c**, Typical $\xi_T(x,y)$ collection fields for TFs with increasing NAs in PBS- fluorescein solution (each field normalized to its maximum); scale bar, 500 μm. **d**, Comparison of the number of photons collected from a two-photon fluorescence spot raster scanned in a PBS-fluorescein solution (pixel dwell time, 3.2 μs) for a FF (inset) and a TF with NA = 0.66 and ψ = ~4°; the isoline in the FF inset shows the maximum number of photons collected by the TF. Scale bar, 500 μm. **e**, Isometric lines of photon collection for a NA-0.66 TF in a PBS-fluorescein solution (top color bar, number of photons per pixel; dwell time, 3.2 μs); isolines are drawn at 10, 20, 50 and 100 photons. Scale bar, 500 μm. **f**, Top, schematic of the far-field imaging system. L1, L2 and L3, imaging lenses; BPF, band-pass filter; NBF, NIR blocker filter; sCOMS, scientific complementary metal-oxyde-semiconductor. Bottom, far-field images of the fiber output facet showing rings of increasing diameter as the source is moved alongside the TF. Scale bar, 0.3 $2\pi/\lambda$. **g**, Transverse vector component k_t of fluorescent light collected by the TF for point-like sources at distance d from the taper tip. Experiments in **a–d** were repeated at least ten times with similar results.

(PMTs) synchronized with the scan head: (i) the microscope PMT, placed in a standard non-descanned, epifluorescence path, and (ii) the fiber PMT, placed at the distal end of a fiber patch connected to the TF[20,21] (Fig. 1b). Once corrected for slight unevenness of the two-photon excitation efficiency in the field of view with the reference image obtained by the microscope PMT, the signal from the fiber PMT reported the fluorescence light collection field of the TF, defined as $\xi_T(x,y)$. We measured collection fields $\xi_T(x,y)$ for fibers with different numerical apertures (NAs) and core diameters, but similar taper angles, ψ, of ~4° (Fig. 1c). We found that the light-sensitive region along the taper, defined as the collection length L, grows with increasing fiber NA and decreasing ψ (Supplementary

Fig. 1a). Therefore, the collection length of a TF can be tailored from a few hundred micrometers up to ~2 mm by modifying the fiber NA and taper angle ψ. This finding reveals an important difference in collection properties of TFs and FFs, because for FFs, the collection depth does not substantially depend on NA[21].

We compared the collection fields for TFs and FFs with NA = 0.66 (Fig. 1d) and 0.39 (Supplementary Fig. 1b), respectively. The optically active surface of TFs extends along the waveguide axis, resulting in relatively uniform collection along the taper. As reflected in the collection fields $\xi_F(x,y)$, FFs collect a higher signal intensity in the vicinity of the end facet. Conversely, the TF collection efficiency profile reaches a lower maximum near the taper surface and follows

a two-lobe shape that widens at the tip (Fig. 1e and Supplementary Figs. 1c,d and 2). In three dimensions, the distribution of the collected signal is fully symmetrical around the taper axis, as seen in the volumetric collection field $\xi(x,y,z)$ (Supplementary Fig. 1d).

This happens because the TF surface optically interfaces with the surrounding environment via modal subsets of increasing transverse propagation component k_t for wider waveguide diameters[27]. Therefore, the full set of propagating modes supported by the straight portion of the fiber is progressively populated along the taper, resulting in a uniform collection along the TF axis. In contrast, all the propagating modes of a FF are coupled at the fiber facet.

To better characterize the physics of light collection by the taper, we imaged the far field of the collected light when fluorescence was stimulated by two-photon excitation from a point-like spot next to the taper surface (Fig. 1f). We found that different modal subsets are populated at specific taper diameters (Fig. 1f,g), as the image on the camera is a ring, the radius of which increases as a function of the distance between the fluorescence source and the taper tip. The ring radius h is a direct measurement of the transversal component k_t of the wave vector associated with guided modes traveling into the fiber[27,28]. Therefore, light entering at different sections of the taper is guided by different subsets of guided modes, and it generates rings with different diameters on the camera, building a correlation between h and the location of the fluorescence signal along the taper.

Uniform collection over large and deep areas. To prove that TFs can be exploited to obtain uniform collection over large and deep brain areas in the presence of scattering and absorption, we measured fluorescence collection fields $\xi(x,y)$ and fluorescence excitation fields $\beta(x,y)$ for FFs and TFs in brain slices uniformly stained with fluorescein. Combining these fields results in the photometry efficiency field $\rho(x,y)$, which describes the dependence of the fluorescence signal on the excitation light intensity[20,21] and thus gives exhaustive geometric information on the sampled tissue volume. We compared collection and photometry fields for FFs and TFs of matching NA and core size. As shown by $\xi_F(x,y)$ and $\rho_F(x,y)$ fields for a FF inserted at the cortex surface (Fig. 2a), FFs effectively interfaced with the superficial layers of the cortex; however, they extracted little information farther than 300 μm from the facet. Conversely, TFs interfaced more uniformly, with brain tissue surrounding the optically active area of the taper (Fig. 2b). Exploiting the symmetry of $\xi(x,y)$, we calculated the volume sampled by the waveguides as a function of the collected signal (Supplementary Fig. 3) and determined the tissue volumes that generated a given fraction of the total collected signals. We found that these volumes tended to be larger for TF than for FF (Supplementary Fig. 4). This is a property that can be exploited in experiments using the full taper surface to excite and collect signals (Fig. 2c).

Reconfigurable multisite collection along the taper. The collection volume of TFs can be dynamically switched among multiple locations along the taper using site-selective light delivery and mode-division demultiplexing strategies[22,27,28]. To define the geometric configuration of volumes that can be addressed, we acquired the $\xi_T(x,y)$ collection field for a 0.66-NA TF inserted in a fluorescein-stained brain slice (Fig. 2d). Using a fast-scanning system based on a galvanometric mirror (Fig. 2e), we injected laser light into the TF by exciting modal subsets with increasing k_t, therefore restricting the illumination volume to confined regions that can be gradually moved along the taper portion by changing the light input angle[22,27,28] (Supplementary Fig. 5a,b). Because fluorescence is only generated in the confined illuminated tissue volume (Supplementary Fig. 5a,b), TFs can dynamically interrogate multiple sites across a functional region. As a proof of principle, we measured the photometry efficiency fields $\rho_T(x,y)$, combining $\xi_T(x,y)$ and $\beta(x,y)$ arising from
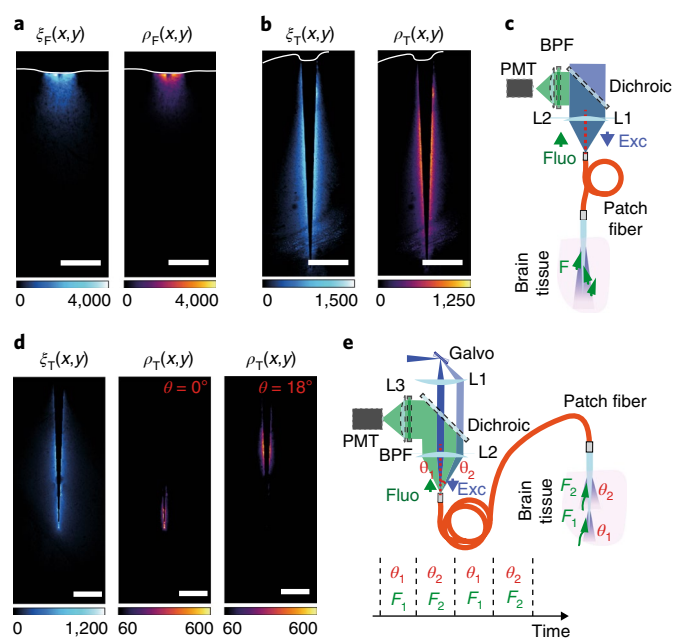

Fig. 2 | Reconfigurable light collection with TFs. a, Light collection field $\xi(x,y)$ (left) and photometry efficiency field $\rho(x,y)$ (right) for a 0.66-NA FF in contact with the cortex of a brain slice uniformly stained with fluorescein. **b**, As in **a** for a 0.66-NA TF inserted in a brain slice uniformly stained with fluorescein. **c**, Schematic of a system using full-NA illumination with blue laser light to stimulate and collect fluorescence from a large brain region. The collected light is back-propagated in the patch fiber and discriminated from blue light by a dichroic mirror that directs it toward a PMT. L1 and L2, lenses; BPF, band-pass filter; Fluo, fluorescence signal; Exc, excitation light. **d**, Site-selective illumination confines the volume sampled to subregions along the TF. Left, light collection field $\xi_T(x,y)$; center, photometry efficiency field $\rho_T(x,y)$ obtained with selective illumination at the fiber tip; right, $\rho_T(x,y)$ field obtained via selective illumination at wider taper diameters. **e**, Schematic of a proposed system for multisite photometry using a PMT detector in a time-division multiplexed configuration. A blue laser beam is launched into a fiber patch cord at increasing input angles (θ_1, θ_2). When injecting at low angles, laser light is outcoupled at the taper tip and generates fluorescence signal F_1; conversely, when injected at θ_2, laser light is outcoupled at larger taper diameters and generates fluorescence signal F_2. The fluorescence light is detected by a PMT, the output signal of which is synchronized with the light injection stimulus. The fluorescence signal is attributed to the appropriate region according to its time stamp. Experiments in **a,b,d** were repeated three times with similar results.

site-selective illumination. $\rho_T(x,y)$ is maximized in confined regions where the location can be inferred from the light injection angle (Fig. 2d). Leveraging this property, the fluorescence signal can be attributed to the brain region that is illuminated using time-division multiplexing (Fig. 2e). This is achieved by launching a laser into a fiber patch cord at increasing input angles (θ_1, θ_2) to excite different modal subsets that are outcoupled at confined positions along the taper. The fluorescence generated for each illumination position (F_1, F_2 respectively) is collected by the taper, back-propagated in the fiber patch cord, discriminated by a dichroic mirror and finally detected by a PMT, the output signal of which is synchronized with the light injection stimulus (Fig. 2e).

To demonstrate that this approach is resilient to modal mixing that might arise from animal movements[22], we monitored the far-field patterns while manually shaking the fiber patch during a depth-resolved photometry measurement in a PBS-fluorescein bath. Recorded intensity fluctuations were <1%, and far-field ring
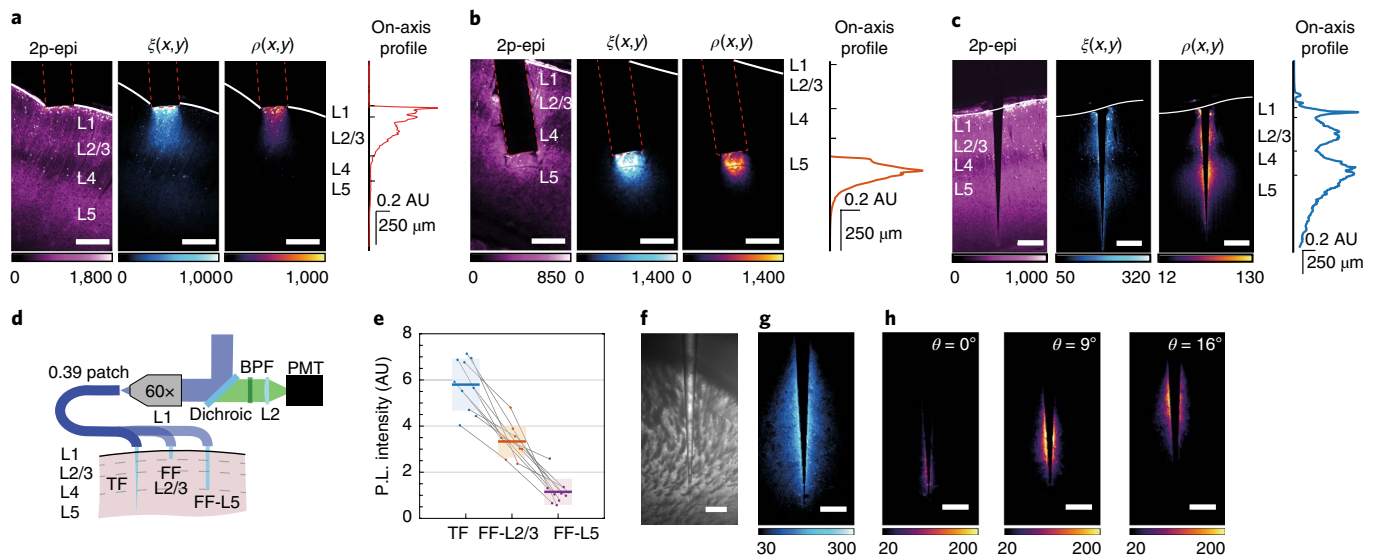
Fig. 3 | Enhanced photometry from genetically stained neural populations. a, Light collection for a 0.39-NA FF at the cortex surface; from left to right: two-photon epifluorescence (2p-epi) image, $\xi(x,y)$ field, $\rho(x,y)$ field, on-axis collection profile $\rho(x,y)$. **b**, As in **a** for a NA = 0.39 FF in proximity of L5. **c**, As in **a,b** for a 0.39-NA TF inserted across the cortical depth. Scale bars (**a**–**c**), 250 μm. **d**, Diagram of the photometry system for the three experimental configurations: a TF inserted across the whole cortex, a FF inserted into L2/3, a FF inserted as deep as L5. **e**, Intensity of the fluorimetry signal ($n = 10$) in slices from *Thy1*-ChR2-EYFP mice using 0.39 TFs ($\psi = 4°$) inserted across the cortex (blue), a 0.39-NA FF inserted in L2/3 (orange) and 0.39-NA FF in L5 (purple) to stimulate and detect fluorescence. Laser power was adjusted to obtain a similar power density from the optically active area of FFs and TFs (0.1 mW mm⁻²). Shaded areas indicate the standard error on the mean. Gray lines connect data obtained in the same experimental run from the same brain slice. Statistical significance was assessed with a two-sided Student *t* test, with significance $\alpha = 0.001$. **f**, Bright-field image of a TF inserted into the striatum in a fixed brain slice (*Thy1*-ChR2-EYFP mouse). **g**, Light collection field $\xi_T(x,y)$ for the TF in **f**. **h**, The combination of the $\xi_T(x,y)$ field with site-selective light delivery generates photometry efficiency fields $\rho_T(x,y)$ that show reconfigurable, multisite light collection from striatal subregions. Scale bars (**f**–**h**), 250 μm. Experiments in **a**–**c**, **g**, **h** were repeated three times with similar results.

diameter and thickness variations were <0.8% (with respect to the unperturbed fiber; Supplementary Fig. 5c,d and Supplementary Videos 1 and 2).

Enhanced fluorimetry in genetically stained neural populations. To illustrate the advantages offered by the extended collection depth of TFs, we used a 0.39-NA TF ($\psi = \sim4°$) and FF to stimulate and detect fluorescence from different cortical layers in fixed brain slices of *Thy1*-ChR2-eYFP mice, where EYFP is limited to L2/3 and L5 (Fig. 3a–c). We measured $\xi(x,y)$, $\beta(x,y)$ and $\rho(x,y)$ fields for three experimental configurations: a FF abutting superficial layers (Fig. 3a), a FF inserted into layer L5 (Fig. 3b) and a TF inserted across the cortical extent (Fig. 3c). As expected, the TF stimulated and collected fluorescence from both layers L2/3 and L5, whereas the FF recruited signal within a confined region near the facet and needed to be repositioned to address both areas. Additionally, the blunt geometric profile of FFs hindered fiber insertion, as displaced tissue remained in front of the facet as the fiber traversed the slice.

We compared the absolute level of signal arising from the three experimental configurations (Fig. 3d), modulating the laser power to compensate for the larger optically active area of TFs and to deliver the same average power density across each optical surface (~0.1 mW mm⁻²). Under these conditions, the TF produced a larger fluorescence signal with respect to the FF at both depths (Fig. 3e), which can be explained by the combined effect of mode-division demultiplexing in light collection and light delivery. Mode-division demultiplexing distributes the higher total illumination power over a wider surface while maintaining a moderate power density[22,27]. As more photons are released into the tissue and more neurons contribute to the collection signal, more fluorescence is generated and detected, consistent with previous findings that TFs elicit optogenetic activation at lower output powers than FFs[22]. Importantly,

because photobleaching depends on the light exposure of each fluorophore, when the full optically active area is engaged, the distribution of light over a larger volume of tissue by TFs allows more fluorescence to be generated without increasing photobleaching.

Spatially resolved photometry in vivo. To gain a deeper understanding of neural processes that underlie motor behavior and reward-driven actions, fiber photometry has been used to probe the activity of striatal neurons[11–13,29]. In this context, TFs extend experimental capabilities by sampling multiple regions with a single, remotely controlled implant. To support this argument, we characterized site-selective fluorimetry with TFs in the striatum (Fig. 3f). We inserted a 0.66-NA TF into the striatum of fixed brain slices from *Thy1*-ChR2-EYFP mice and, after acquiring the $\xi(x,y)$ field (Fig. 3g), we used site-selective illumination to produce photometry efficiency $\rho(x,y)$ fields for increasing input angles (Supplementary Fig. 5). As expected, the volume that responds to site-selective illumination gradually moved away from the TF tip as the light input angle increased (Fig. 3h).

We tested the TF system in vivo by simultaneously measuring dopamine transients using dLight1.1 (ref. [30]) from dorsal and ventral striatum, two brain regions that show distinct dopamine signals[31]. We trained mice in a simple operant conditioning paradigm, during which we collected dLight fluorescence from dorsal and ventral striatum (Fig. 4a, NA = 0.39). In this paradigm, a mouse had to remain in one side of the chamber to trigger delivery of a food reward from a receptacle located on the other side of the chamber. This forced the mouse to run from one side of the chamber to the other to collect the reward and to stop moving while consuming the reward from the receptacle.

We observed classical reward-driven dopamine transients in ventral striatum, whereby dLight fluorescence increased during rewarded receptacle entries and decreased during unrewarded
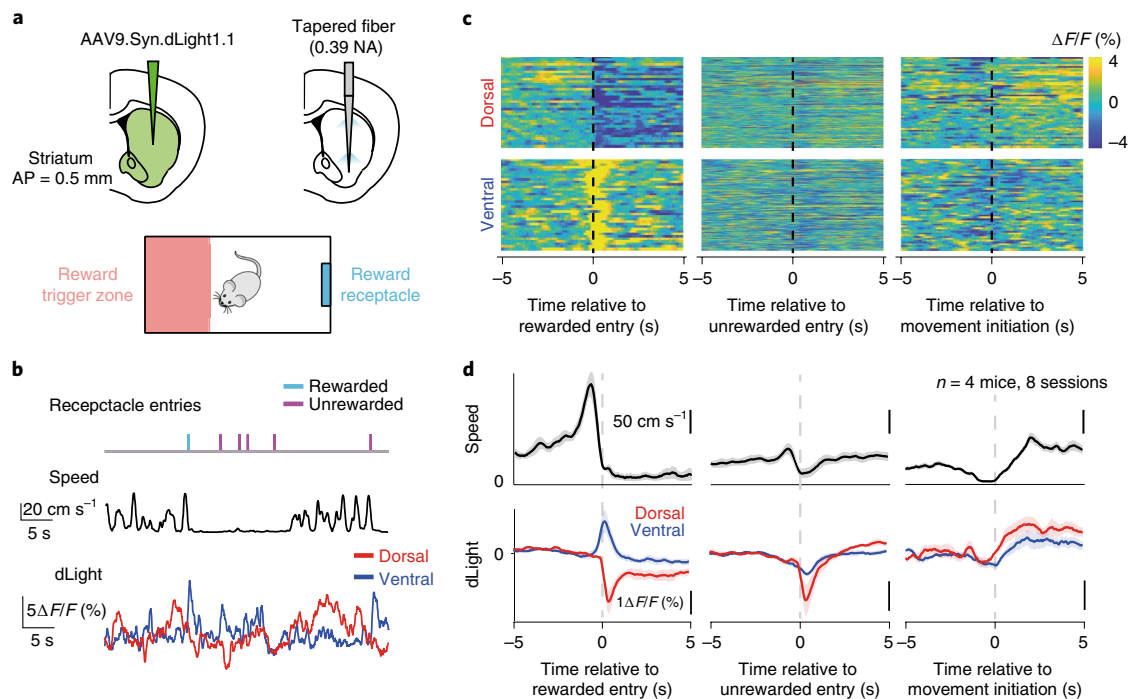
Fig. 4 | In vivo multipoint photometry reveals distinct dopamine responses to locomotion and reward in dorsal and ventral striatum. a, Top, schematics of a surgical site and two-site TF illumination for in vivo fiber photometry. Bottom, schematic of the behavior chamber. The red zone indicates the area of the box in which the mouse needs to enter to trigger delivery of a food pellet in the receptacle (blue). After reward delivery, a minimum time of 30 s needs to elapse before another reward can be delivered. **b**, Example photometry signals from one mouse. Top, behavioral time stamps measured by an infrared beam break in the receptacle. Cyan, rewarded receptacle entry; magenta, unrewarded receptacle entry. Middle, centroid speed of the animal. Bottom, dLight photometry signals. Red, signal from the dorsal site; blue, signal from the ventral site. **c**, Heat maps of dLight photometry signals from all trials from an example mouse (two sessions). Top, signal from the dorsal site. Bottom, signal from the ventral site. Each row represents an individual trial. $n = 37$ trials for rewarded receptacle entry. $n = 435$ trials for unrewarded receptacle entry. $n = 52$ trials for movement initiation. **d**, Average speed and dLight photometry signals from all sessions across mice. Signals from the dorsal site are shown in red; signals from the ventral site are shown in blue ($n = 8$ sessions from four mice). Shaded areas represent the standard error on the mean of the session averages.

entries (Fig. 4b–d; all trials shown separately for individual mice in Supplementary Fig. 6). However, dorsal dLight fluorescence decreased for both rewarded and unrewarded receptacle entries, suggesting that dopamine release in dorsal striatum is more highly correlated with changes in movement rather than the acquisition of reward (Fig. 4b–d). Furthermore, the signs of behaviorally induced changes in dopamine were opposite for dorsal and ventral striatum at the time of rewarded receptacle entry and, consistent with a function of dopamine in movement initiation[32,33], signals in both sites increased during movement initiations (Fig. 4b–d). Thus, although both dorsal and ventral striatum dopamine transients track locomotion, only those in ventral striatum respond strongly to rewards.

Engineering collection volumes with microstructured TFs. The large surface over which TFs interface with the environment permits engineering the collection volume according to the region of interest (Fig. 5). This can be achieved using micro- and nanofabrication technologies to structure the fiber taper, as it has been shown for light delivery[25,26,34]. Here we show: (i) the restriction of light collection to a specific angular extent around the waveguide (Fig. 5a–d), (ii) the observation of cell bodies in deep cortical layers while light collection is restricted to a specific spot along the taper (Fig. 5e–l), (iii) selective illumination and collection from two optical windows that are individually addressed by manipulating the excitation laser beam (Fig. 5m,n)

To confine light collection to a half-portion of the waveguide surface, we thermally evaporated a highly reflective aluminum layer

on the opposite side (Fig. 5a). The collection fields $\xi(x,y)$ (Fig. 5b) and profile along the optical surface of the half-coated TF (Fig. 5c) were similar to those of an uncoated twin probe, both in terms of shape and of collected number of photons. Therefore, the metal coating does not substantially change the detected signal, suggesting that nearly all photons entering the uncoated taper undergo dielectric total internal reflection, a condition that is forced by the metal layer in the half-coated fiber. We tested the side-collection properties of the device in tissue with the half-coated TF inserted into a fixed brain slice expressing EYFP under control of the *Thy1* promoter (Fig. 5c). We acquired a two-photon epifluorescence image and the $\xi(x,y)$ field and found that, despite generating fluorescence all around the fiber, only fluorescence that arose close to the uncoated portion of the fiber was acquired by the fiber PMT (Fig. 5d).

Light collection from optical windows at arbitrary depth. We explored the possibility of further restricting the collection volume by fabricating optical windows on a TF entirely coated with aluminum. We used focused ion beam milling to selectively remove the metal in specific regions of the taper[25,26]. To optimize the devices, we characterized light collection from optical windows in PBS-fluorescein solution (30 μM), as described above. We fabricated probes (NA = 0.39) with squared optical windows of different side lengths ($W = 60$, 30, and 15 μm) positioned at different distances from the fiber tip ($L = 230$, 750, and 1,250 μm) (Fig. 5e,f). The volumetric collection diagrams for these devices (Supplementary Fig. 7a) revealed that larger windows resulted in larger collection
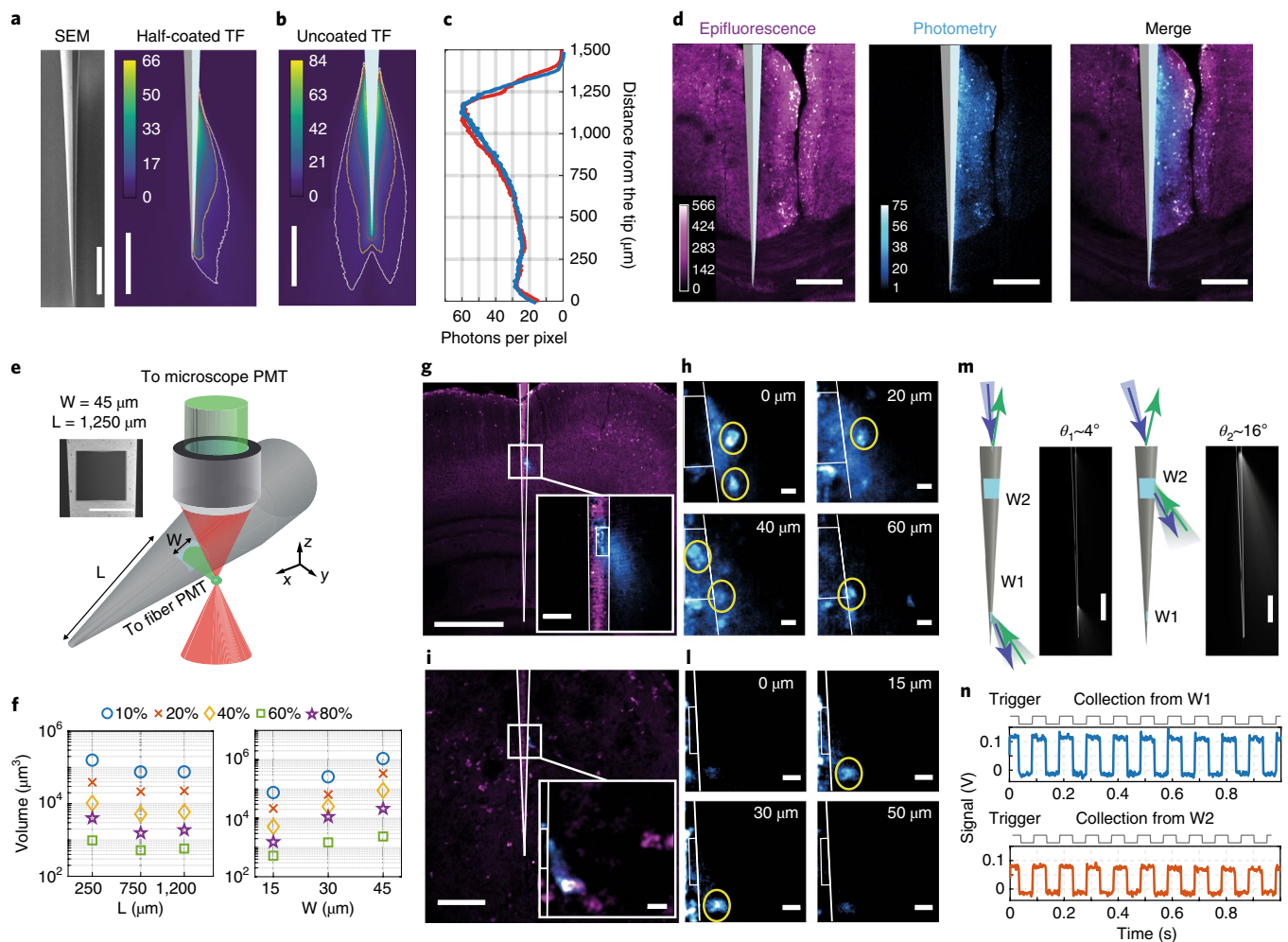
Fig. 5 | Engineering the light collection volume with microstructured TFs. a, Left, Scanning electron micrograph (SEM) of a half-metallicized TF. Right, $\xi(x,y)$ field for a half-coated 0.39-NA TF in PBS-fluorescein solution. **b**, $\xi(x,y)$ field for an uncoated 0.39-NA TF in PBS-fluorescein solution. Isolines represent 5, 10, and 20 photons per pixel in white, yellow and red, respectively (dwell time, 3.2 µs). **c**, $\xi(x,y)$ field profiles for a half-coated TF (red) and an uncoated TF (blue). **d**, Collection from a half-coated TF in a fixed brain slice (*Thy1*-ChR2-EYFP mouse). Left to right: two-photon epifluorescence, $\xi(x,y)$ field, merged epifluorescence (magenta) and $\xi(x,y)$ (cyan). Scale bars (**a**–**d**), 250 µm. **e**, Setup used to characterize light collection from optical windows. Inset, SEM micrograph of a square window ($W = {\sim}45\,\mu m$, $L = {\sim}1{,}250\,\mu m$). **f**, Collection volumes in PBS-fluorescein solution enclosed by collection isosurfaces versus L and W. Isosurfaces are at 10%, 20%, 40%, 60%, 80% of the maximum (Supplementary Fig. 6). **g**, Light collection from a square window ($W = {\sim}45\,\mu m$, $L = {\sim}750\,\mu m$) in a fixed brain slice (*Thy1*-ChR2-EYFP mouse); the image shows the overlay of the $\xi(x,y)$ field (cyan) with a simultaneously acquired two-photon epifluorescence image (magenta); scale bar, 500 µm. Inset, zoom-in on the window; scale bar, 50 µm. **h**, Z-stack at increasing height above the optical window (0, 20, 40, 60 µm). The TF profile and window position are outlined in white. Scale bar, 10 µm. **i**, As in **g**, for a TF with a window of $W = {\sim}20\,\mu m$, $L = {\sim}230\,\mu m$; scale bars, 100 µm (inset, 10 µm). **l**, As in **h**, for a $W = {\sim}20\,\mu m$ optical window: z-stack at heights 0, 15, 30, 50 µm; scale bar, 10 µm. **m**, Setup used for site-selective illumination and collection. The TF is submerged in a PBS-fluorescein drop. Laser beam pulses (10 Hz, 50 ms, 473 nm) are injected at controlled θ (Supplementary Fig. 7c). Scale bar, 500 µm. **n**, Fluorescence signal measured from windows W1 and W2, independently activated by manipulating θ (fluorescence signals corrected by subtracting autofluorescence). Experiments in **c**,**d**,**g**–**l**,**n** were repeated three times with similar results.

volumes (Fig. 5f). However, although a window near the tip collected from a slightly larger volume, windows at larger taper sections had similar collection properties (Fig. 5f).

We tested the optical performances of microstructured TFs in fixed brain slices from a *Thy1*-ChR2-EYFP mouse by acquiring $\xi(x,y)$ fields that we correlated with simultaneous epifluorescence imaging. We found that for a TF with a window of width $W = {\sim}45\,\mu m$ positioned at $L = {\sim}750\,\mu m$ from the taper tip, light collection colocalized with the optical window location, with a collection lobe that was not perpendicular to the fiber axis but directed toward the taper tip (Fig. 5g). This property ties in well with selective light delivery from optical windows[25], because it allows interfacing with cellular volumes at depth with high spatial selectivity

(Fig. 5h). Furthermore, a 3D fluorescence stack acquired from a region adjacent to an optical window (side $W = {\sim}45\,\mu m$, $L = {\sim}750\,\mu m$ from the tip) (Fig. 5h and Supplementary Fig. 7b) showed an exact match between photometry diagrams and epifluorescence imaging. We obtained similar results using a TF with windows of $W = {\sim}25\,\mu m$ in width, located at $L = {\sim}230\,\mu m$ from the tip (Fig. 5i,l).

As we have shown for uncoated TFs, mode-division demultiplexing strategies can be exploited to selectively excite and collect fluorescence from two optical windows fabricated at different sections of the same TF (Fig. 5m and Supplementary Fig. 7c). To do this, we submerged a microstructured TF in a fluorescein drop, and we injected a laser beam (473 nm) at different input angles to select one window at a time (Supplementary Fig. 7c). We measured the
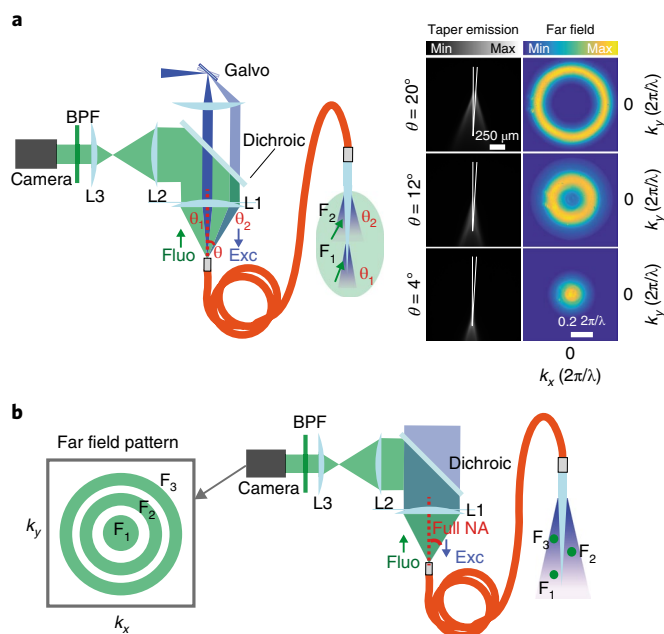
Fig. 6 | Detection schemes exploiting far-field imaging for depth-resolved fiber photometry. a, Time-division multiplexing can be supported by far-field detection of fluorescence to improve depth selectivity. **b**, Far-field detection can be implemented with full-NA stimulation, enabling pure mode-division demultiplexing based on the k_T value of back-propagated fluorescence. Fluo, fluorescence signal; Exc, excitation light.

collected fluorescence signal with a photodetector while modulating the laser power with an Acousto-Optic Modulator (10 Hz, 50% duty cycle square wave) (Fig. 5n). Fluorescence was selectively excited at each window location, demonstrating that TF can selectively illuminate and collect light from two confined regions (Fig. 5m,n and Supplementary Fig. 7c).

Discussion

Acquiring fluorescence signals from activity indicators expressed in the brain is a powerful technique in neuroscience[35,36], and the field would greatly benefit from an implantable waveguide system that can be configured to efficiently and selectively collect light from regions of interest. Additionally, the methodology presented in this manuscript can open further perspectives in the use of far-field detection to obtain depth selectivity in fiber photometry experiments (Fig. 6).

We envision that the application of TF probes to collect fluorescence from scattering tissue will facilitate dissecting the contribution of multiple functional areas in deep brain regions while providing a versatile complement to existing optical methods. Photometry approaches based on mode-division demultiplexing from TFs can also potentially extend to the large class of soft, biologic, live tissue, of which the brain represents one of the most challenging cases in terms of scattering properties, considering both scattering length and anisotropy. In this framework, TFs add beneficial features to the existing set of devices for light collection, with an ensemble of different configurations that is not achievable with either FFs or μLED/ photodetectors systems[10].

Online content

Any methods, additional references, Nature Research reporting summaries, source data, statements of code and data availability and associated accession codes are available at https://doi.org/10.1038/s41592-019-0581-x.

References

1. Peterka, D. S., Takahashi, H. & Yuste, R. Imaging voltage in neurons. *Neuron* **69**, 9–21 (2011).
2. Luo, L., Callaway, E. M. & Svoboda, K. Genetic dissection of neural circuits: a decade of progress. *Neuron* **98**, 256–281 (2018).
3. Stroh, A. et al. Making waves: initiation and propagation of corticothalamic Ca²⁺ waves in vivo. *Neuron* **77**, 1136–1150 (2013).
4. Schwalm, M. et al. Cortex-wide BOLD fMRI activity reflects locally-recorded slow oscillation-associated calcium waves. *eLife* **6**, e27602 (2017).
5. Adelsberger, H., Grienberger, C., Stroh, A. & Konnerth, A. In vivo calcium recordings and channelrhodopsin-2 activation through an optical fiber. *Cold Spring Harb. Protoc.* **2014**, pdb.prot084145 (2014).
6. Fuhrmann, F. et al. Locomotion, theta oscillations, and the speed-correlated firing of hippocampal neurons are controlled by a medial septal glutamatergic circuit. *Neuron* **86**, 1253–1264 (2015).
7. Simone, K., Füzesi, T., Rosenegger, D., Bains, J. & Murari, K. Open-source, cost-effective system for low-light in vivo fiber photometry. *Neurophotonics* **5**, 025006 (2018).
8. Muir, J. et al. In vivo fiber photometry reveals signature of future stress susceptibility in nucleus accumbens. *Neuropsychopharmacology* **43**, 255–263 (2018).
9. Adelsberger, H., Zainos, A., Alvarez, M., Romo, R. & Konnerth, A. Local domains of motor cortical activity revealed by fiber-optic calcium recordings in behaving nonhuman primates. *Proc. Natl Acad. Sci. USA* **111**, 463–468 (2014).
10. Lu, L. et al. Wireless optoelectronic photometers for monitoring neuronal dynamics in the deep brain. *Proc. Natl Acad. Sci. USA* **115**, E1374–E1383 (2018).
11. Meng, C. et al. Spectrally Resolved fiber photometry for multi-component analysis of brain circuits. *Neuron* **98**, 707–717.e4 (2018).
12. Cui, G. et al. Concurrent activation of striatal direct and indirect pathways during action initiation. *Nature* **494**, 238–242 (2013).
13. Markowitz, J. E. et al. The striatum organizes 3D behavior via moment-to-moment action selection. *Cell* **174**, 44–58 (2018).
14. Kim, C. K. et al. Simultaneous fast measurement of circuit dynamics at multiple sites across the mammalian brain. *Nat. Methods* **13**, 325–328 (2016).
15. Gunaydin, L. A. et al. Natural neural projection dynamics underlying social behavior. *Cell* **157**, 1535–1551 (2014).
16. Schmid, F. et al. Assessing sensory versus optogenetic network activation by combining (o)fMRI with optical Ca²⁺ recordings. *J. Cereb. Blood Flow. Metab.* **36**, 1885–1900 (2016).
17. Lütcke, H. et al. Optical recording of neuronal activity with a genetically-encoded calcium indicator in anesthetized and freely moving mice. *Front. Neural Circuits* **4**, 9 (2010).
18. Guo, Q. et al. Multi-channel fiber photometry for population neuronal activity recording. *Biomed. Opt. Express* **6**, 3919 (2015).
19. Cui, G. et al. Deep brain optical measurements of cell type–specific neural activity in behaving mice. *Nat. Protoc.* **9**, 1213–1228 (2014).
20. Tai, D. C. S., Hooks, D. A., Harvey, J. D., Smaill, B. H. & Soeller, C. Illumination and fluorescence collection volumes for fiber optic probes in tissue. *J. Biomed. Opt.* **12**, 034033 (2007).
21. Pisanello, M. et al. The three-dimensional signal collection field for fiber photometry in brain tissue. *Front. Neurosci.* **13**, 82 (2019).
22. Pisanello, F. et al. Dynamic illumination of spatially restricted or large brain volumes via a single tapered optical fiber. *Nat. Neurosci.* **20**, 1180–1188 (2017).
23. Park, S. et al. One-step optogenetics with multifunctional flexible polymer fibers. *Nat. Neurosci.* **20**, 612–619 (2017).
24. Acker, L., Pino, E. N., Boyden, E. S. & Desimone, R. FEF inactivation with improved optogenetic methods. *Proc. Natl Acad. Sci. USA* **113**, E7297 (2016).
25. Pisanello, F. et al. Multipoint-emitting optical fibers for spatially addressable in vivo optogenetics. *Neuron* **82**, 1245–1254 (2014).
26. Pisano, F. et al. Focused ion beam nanomachining of tapered optical fibers for patterned light delivery. *Microelectron. Eng.* **195**, 41–49 (2018).
27. Pisanello, M. et al. Tailoring light delivery for optogenetics by modal demultiplexing in tapered optical fibers. *Sci. Rep.* **8**, 4467 (2018).
28. Pisanello, M. et al. Modal demultiplexing properties of tapered and nanostructured optical fibers for in vivo optogenetic control of neural activity. *Biomed. Opt. Express* **6**, 4014 (2015).
29. Klaus, A. et al. The spatiotemporal organization of the striatum encodes action space. *Neuron* **95**, 1171–1180 (2017).
30. Patriarchi, T. et al. Ultrafast neuronal imaging of dopamine dynamics with designed genetically encoded sensors. *Science* **360**, 1420 (2018).
31. Howe, M. W. & Dombeck, D. A. Rapid signalling in distinct dopaminergic axons during locomotion and reward. *Nature* **535**, 505–510 (2016).

32. Coddington, L. T. & Dudman, J. T. Emergence of reward expectation signals in identified dopamine neurons. *Nat. Neurosci.* **21**, 1563–1573 (2018).
33. da Silva, J. A., Tecuapetla, F., Paixão, V. & Costa, R. M. Dopamine neuron activity before action initiation gates and invigorates future movements. *Nature* **554**, 244–248 (2018).
34. Rizzo, A. et al. Laser micromachining of tapered optical fibers for spatially selective control of neural activity. *Microelectron. Eng.* **192**, 88–95 (2018).
35. Tanese, D. et al. Imaging membrane potential changes from dendritic spines using computer-generated holography. *Neurophotonics* **4**, 031211 (2017).
36. Wang, T. et al. Three-photon imaging of mouse brain structure and function through the intact skull. *Nat. Methods* **15**, 789–792 (2018).

Author contributions
F. Pisano and M.P. equally contributed to this work. F. Pisano, M.P., A.B., M.B., B.L.S. and F. Pisanello developed the optical systems for the characterization of TFs. F. Pisano, M.P., E.M, A.B., M.B. and B.S. performed optical characterization of TF and ex vivo experiments. F. Pisano, M.P. and A.B. analyzed the data from ex vivo experiments. J.L. and S.J.L. developed the in vivo scanning TF photometry system, performed the in vivo experiment and analyzed the in vivo data. F. Pisano, L.S. fabricated the microstructured TFs. M.H. and F. Pisanello performed preliminary experiments. F. Pisano, M.P, J.L, S.J.L, B.L.S., M.D.V. and F. Pisanello wrote the manuscript and prepared the figures with contributions from all authors. M.D.V., B.L.S. and F. Pisanello conceived the study and jointly supervised the work.

Competing interests
L.S., M.D.V., B.L.S. and F. Pisanello are founders and hold private equity in OptogeniX, a company that develops, produces and sells technologies to deliver light into the brain. Tapered fibers commercially available from OptogeniX were used as tools in the research.

Additional information
Supplementary information is available for this paper at https://doi.org/10.1038/s41592-019-0581-x.

Correspondence and requests for materials should be addressed to F.P., M.D.V., B.L.S. or F.P.

Peer review information Nina Vogt was the primary editor on this article and managed its editorial process and peer review in collaboration with the rest of the editorial team.

Reprints and permissions information is available at www.nature.com/reprints.

Publisher's note Springer Nature remains neutral with regard to jurisdictional claims in published maps and institutional affiliations.

Methods

Optical setup for characterizing TF light collection properties. A custom two-photon laser scanning microscope was implemented to characterize TF light collection fields $\xi(x,y,z)$ and light emission fields $\beta(x,y,z)$. The apparatus is similar to previously described systems[20,21]. Briefly, the optical setup consisted of a scanning path followed by an upright microscope. A femtosecond-pulsed near-infrared laser beam (Chameleon Discovery, Coherent) was directed toward a power modulation system composed of a half-wave plate, a polarizing cube and a Pockels Cell (Conoptics 350-80-02). Then, a periscope raised the laser beam, and a quarter-wave plate (Thorlabs AQWP05M-980) produced a circular polarization. A beam expander enlarged the laser beam before relaying it into a galvanometric scan system (Sutter). The scanned beam was then reflected toward the back aperture of an objective mounted on an upright Olympus BX-61 microscope aligned with the scanning path. A piezoelectric motor (Phisik Instrument P-725.4CD) was used to control the objective z position, allowing volumetric scanning. An epifluorescence detection system was set using a dichroic mirror (Semrock FF665-Di02) positioned above the objective to reflect fluorescent light toward a non-descanned PMT, referred to as the 'microscope' PMT (Hamamatsu H10770PA-40). Light was focused on the PMT window with a lens system and filtered (BPF, Semrock FF01-520/70-25). Image acquisition was controlled via commercial software (ScanImage, Vidrio Technologies). Images were acquired in 512×512 pixels, with a 3.2-μs pixel dwell time. Laser power and scanning range were adjusted at convenience. Wide-field (Figs. 1–3 and 5a,b,d,g,i) were acquired with a ×4 objective (Olympus XLFluor ×4/340a); high-resolution images (Fig. 5h,l) were obtained with a ×25 objective (Olympus XLPLN25XWMP2). When necessary, image stitching was performed with FIJI software[37].

Light collection fields $\xi(x,y)$. Light collection fields were measured for TFs and FFs submerged in a semi-transparent solution (PBS-fluorescein 30 μM) or inserted in brain slices. An endoscopic detection system was implemented to detected fluorescent light collected by the fibers when the focal spot was raster-scanned in their surroundings. To do this, the fibers were connected to a fiber patch via ferrule-to-ferrule butt coupling. Light emitted at the distal end of the fiber was collected with a high-NA objective (Olympus Plan N ×40). The output of the objective was routed to a second PMT, referred to as the 'fiber' PMT (Hamamatsu H7422P-40) after passing through two spherical lenses (Thorlabs LA1050-A and LA1805-A) and a band-pass filter (Semrock FF03-525/50-25). Collection fields $\xi(x,y)$ were obtained by averaging out 60 acquisitions. Volumetric collection fields $\xi(x,y,z)$ were produced by recording the fiber output during volumetric scanning. Light collection fields in brain tissue were acquired by inserting the TF into brain slices positioned in the sample plane. Fiber insertion was controlled with a micromanipulator (Scientifica) upon live imaging with a sCMOS camera. Light collection fields from optical windows in fluorescein and brain slices were obtained by scanning the two-photon fluorescent spot with a high-magnification ×25 objective (Olympus XLPLN25XWMP2) in the vicinity of the window.

Light emission fields $\beta(x,y)$. To measure light emission fields $\beta(x,y,z)$, laser light (473 nm) was injected at the distal end of the fiber patch. For full-NA light emission[22,27], light was coupled across the whole NA of the fiber patch using a high-NA microscope objective (Olympus Plan N ×40) (Fig. 2c); for site-selective illumination, light was injected using a scanning system based on a galvanometric mirror[22,27] (Fig. 2e). The optical system was equipped with two detection paths to image the light emission field, primarily in brain tissue.

Because the optical system houses a confocal scanning path alongside the two-photon path, the detection was rearranged to direct fluorescent light excited by the fiber emission toward a descanned pinhole system (Thorlabs MPH16). This was done where bleaching effects had limited effect, such as in the case of fluorescein staining. Light passing through the pinhole aperture was detected by a PMT, the 'pinhole' PMT, synchronized with the galvo scanning. This approach has the advantage of providing emission fields whose photon-to-pixel assignation intrinsically replicates the one used for $\xi(x,y,z)$ fields, thus avoiding rescaling and interpolation in image registration. However, the image formed by the objective needs to be scanned several times across the pinhole. This method increases illumination time and potentially results in fluorescence bleaching.

Therefore, in genetically stained brain slices, the emission fields were acquired by redirecting the dichroic mirror toward a CCD camera in bright-field mode. While this approach needs image rescaling to align emission and collection fields, is advantageous to avoid bleaching, as all pixels are acquired simultaneously.

Photometry efficiency fields $\rho(x,y)$. Photometry efficiency fields were calculated by scaling the collection field $\xi(x,y)$ against the normalized illumination field $\beta(x,y)$. Following the approach outlined in ref. [21], the photometry field was calculated as

$$\rho(x,y) = \xi(x,y) \times \beta(x,y)$$

where × indicates pixel-by-pixel multiplication. $\xi(x,y)$ and $\beta(x,y)$ fields were registered manually using FIJI software. The inside portion of the TF was masked, because the information arising from it might suffer aberrations due to the tissue-glass interface. Photometry efficiency fields were calculated with custom code.

Tapered fiber fabrication. Tapered fiber stubs fabricated from fiber cords with NA = 0.22, core/cladding = 50/125 μm (Thorlabs FG050UGA), NA = 0.39, core/cladding = 200/225 μm (Thorlabs FT200UMT), NA = 0.66, core/cladding = 200/230 μm (Plexon PlexBright High Performance patch cable) were obtained from OptogeniX (www.optogenix.com). Details of the fabrication procedure have been described previously[22,38]. Fibers were connected to metallic ferrules with a diameter of 1.25 mm to minimize autofluorescence effects. Half-coated fibers were fabricated by thermally evaporating 600–800 nm of Al on one side of the tapered section. This was done by exposing only one side of the fiber to the crucible. Optical windows were realized with Focused Ion Beam (FIB) milling on TF entirely coated with Al. Briefly, a uniform Al layer was deposited on the TF via thermal evaporation. To obtain a uniform coating, the fibers were mounted on a rotating motor. Optical windows of different sizes were fabricated by removing the metal coating at specific taper diameter using a dual beam FIB-SEM system (FEI Helios Nanolab 600i Dual Beam). In order to remove only the metal coating, without affecting the glass, focused ion beam milling was supervised via simultaneous SEM imaging.

Brain slices. Brain slices were obtained from wild-type mice and *Thy1*-ChR2-EYFP mice. Mouse brains were fixed in 4% PFA and cut with a vibratome in 300-μm-thick slices. Slices from wild-type animals (CL56BL/6) were permeabilized in 0.3% Triton X (Sigma Aldrich) for 30 min, washed in PBS (three 5-min washes), immersed in 1 mM fluorescein solution overnight and washed again (three 5-min washes). All animals were cared for and used in accordance with guidelines of the US Public Health Service Policy on Humane Care and Use of Laboratory Animals and the NIH Guide for the Care and Use of Laboratory Animals. Animal experiments were approved by the Harvard Medical Area Standing Committee on Animals.

Fluorimetry measurements in genetically stained neural populations. Blue laser light (473 nm, Laser Quantum Ciel) was injected over the full NA of a 0.39-NA fiber patch using a microscope objective (Olympus Plan N ×40). The patch was connected to FF and TF stubs via ferrule-to-ferrule butt coupling. These stubs were inserted into the brain slices using a micromanipulator (Scientifica), with the guidance of simultaneous two-photon imaging. The intensity of the fluorescence signal emitted by the brain slice was monitored with two-photon imaging to ensure that all measurements were performed in similar conditions.

Fluorimetry measurements were performed by exciting and collecting fluorescence signal from genetically stained neural populations via the FF and TF stubs. The collected fluorescence signal was discriminated with a short-pass dichroic mirror, a fluorescence filter (Semrock FF03-525/50-25) and detected with the fiber PMT. The PMT signal was amplified and digitized with a data acquisition board (NiDAQ USB-6363) that was controlled with custom software (LabView).

In order to obtain a similar output power density from TF and FFs across all measurements, $\rho_{P,\text{flat}} = \rho_{P,\text{taper}} = \rho_P = 0$, 1 mW/mm^2, laser power was modulated according to the fiber output surface. Power density $\rho_{P,\text{flat}}$ for FFs was calculated as

$$\rho_{P,\text{flat}} = 4 \times P_{\text{flat}} / \pi d_{\text{facet}}^2$$

where P_{flat} is the input power and d_{facet} is the fiber diameter (200 μm).

Power density $\rho_{P,\text{taper}}$ for TFs was instead calculated as

$$\rho_{P,\text{taper}} = \frac{2 P_{\text{taper}}}{\pi (\text{FED})^2 \sqrt{1 + \cot^2(\psi/2)}}$$

where P_{taper} is the input power, FED is the first diameter of emission (125 μm), ψ is the taper angle and clear meaning of the subscripts.

We performed ten measurements for each of the three experimental configurations: FF in L2/3, FF in L5, and TF across the whole cortex (Fig. 3d). Fluorescence signal was acquired for 10 s, at 1,000 samples/s, and binned in 100-ms intervals. Fig. 3e shows the mean value of the three acquisitions for each measurement; error bars are smaller than the data point size.

This produced a population of ten signal values for the three different configurations, from here, referred to as T, F_{placed}, F_{in} respectively for taper, flat placed and flat inserted).

In order to quantitatively compare the total signal collected from the tapered fibers with the one collected by the flat fibers (at the same illumination power density) we performed a two-tailed t test between the two hypotheses:

$$H_0: \overline{T} - \overline{F}_{\text{placed}} = 0 \tag{1}$$

$$H_1: \overline{T} - \overline{F}_{\text{placed}} > 0 \tag{2}$$

where $\overline{T}$, $\overline{F}_{\text{placed}}$ are the mean values for the respective populations. We built a statistic variable $t = \frac{\overline{T} - \overline{F}_{\text{placed}}}{\sqrt{\sigma_T^2 + \sigma_F^2}}$ where σ_T^2, σ_F^2 are standard errors on the mean values, obtaining $t = 5.88$. We rejected the null hypothesis H_0, with a significance level $\alpha = 0,001$ with 18 degrees of freedom. The same procedure was applied to $\overline{T}$ and $\overline{F}_{\text{in}}$

obtaining $t = 11.62$ and rejecting H_0, with a significance level $\alpha = 0.001$ with 18 degrees of freedom. Data analysis was performed with custom code.

Surgery for tapered fiber implantation. A craniotomy was performed in male mice (C57BL/6J from the Jackson Laboratory, ~9 weeks old) above the striatum (+0.5 mm, +1.5 mm lateral to bregma). AAV9.Syn.dLight1.1 (~1−3 × 10¹³ GC/ml) was injected at two different depths (4.0 mm and 2.0 mm, 4.0 µl per site, deeper site first) at 100 nl/min. A single TF (0.39 NA, 200 µm core, 225 µm cladding, 2.5 mm emitting length, 5 mm total length, obtained from OptogeniX) was implanted such that the tip of the fiber was placed at a depth of 3.8 mm. Fiber implants were fixed to the skull surface using Loctite glue and dental cements. Animal experiments were approved by the Harvard Medical Area Standing Committee on Animals.

Behavioral experiments. Mice were placed inside an 8 × 16–inch box chamber (12 inches high) with a food pellet receptacle. Food pellets (20 mg) (Bioserv F05301) were delivered when mice entered a reward trigger zone, located on the opposite side of the box as the receptacle (Fig. 4a). This separation prevented the mice from staying at the receptacle to collect food and allowed measurement of signals during locomotion start and stop. Mice had to wait at least 30 s after a reward delivery to trigger the next reward. Head entries into the receptacle were detected by an infrared sensor installed inside the receptacle. Body position was detected by a camera-based image recognition software (Bonsai). Animals were habituated to the arena for one session before data were collected in two recording sessions. Each session lasted for approximately 20 min.

Optical setup for photometry experiments. A simple setup was used to record signals in dorsal and ventral sites in striatum simultaneously. Briefly, a scanning galvanometer mirror (Cambridge Technologies) moved back and forth every 20 ms between two angular deflections that resulted in 0° and 22° degree injection angles for a laser beam into a 200-µm patch cord (0.39 NA, Doric). The shallow (0°) angle resulted in laser emission from the tapered tip in the ventral striatum, whereas 22° resulted in light emission into the dorsal striatum from a site near the top of the taper. Emission light was spectrally separated from excitation light by a dichroic mirror (Semrock FF496-SDi01) and collected by a PMT (R3896, Hamamatsu), with resulting currents converted to voltage using a trans-impedance amplifier (Stanford Research Systems, SR570). The optical setup was controlled with custom code.

Dopamine signals data analysis. Dorsal and ventral site signals were separated out by averaging the signal in the last 10 ms of each 20-ms illumination period at each site. Parsed raw data (40-ms time bins) were smoothed using a moving average filter (400 ms). $\Delta F/F(\%)$ was calculated relative to the signal (F_0) averaged in the 10 s preceding the time alignment. In terms of a behavioral analysis, we defined a movement initiation time point as times when the animal transitioned from periods of inactivity (>1 s of average speed <10 cm/s and average acceleration <10 cm/s²) to movement (>2 s of average speed >60 cm/s). Data analysis was made with custom code.

Resilience of multipoint fiber photometry with TF to fiber perturbations. A 0.39 NA, 200 µm core TF was submerged in a PBS-fluorescein solution (30 µM). Laser light (473 nm) was injected in a patch cord with matching core size and NA. Fluctuations in laser power were stabilized with a feedback loop established between an Acousto-Optic Modulator (AA Optoelectronics), which controlled the laser power, and a photodetector, receiving a fraction of the excitation beam. Fluorescence was stimulated at specific sections of the TF. The collected light was imaged in far field, where it generated collection rings. The diameter of these

rings is a direct measurement of the transverse propagation component k_t of the collected light. As shown in Supplementary Videos 1 and 2, the fiber was manually perturbed beyond reasonable scenarios in small-animal experiments. Data collection and analysis were made with custom code.

Multipoint fluorimetry from a microstructured TF with two optical windows. A 0.39 NA, 200 µm core, microstructured TF with two optical windows was submerged in a PBS-fluorescein solution (30 µM). Pulses of laser light were generated with an Acousto-Optic Modulator (10 Hz, 50 ms) and injected into the fiber at controlled input angles $\theta_1 \sim 4$ and $\theta_2 \sim 16$ that respectively directed laser light to a single window: W_1, closer to the tip, or W_2, farther from the tip. The fluorescence signal, collected through the optical windows was discriminated with a dichroic mirror and sent to a photodetector (Newport) after filtering out blue light with a fluorescence filter (Semrock FF03-525/50-25). Autofluorescence contribution was measured by performing the same experiment in air and was then subtracted from the acquired signal. Data collection and analysis were made with custom code.

Statistics. Detailed information on statistics used in this work are reported in the captions of the relevant figures and in the Life Sciences Reporting Summary.

Reporting Summary. Further information on research design is available in the Nature Research Reporting Summary linked to this article.

Data availability
Data are available upon reasonable request from the corresponding authors. Data on optical properties of TFs and optical measurements are available from F. Pisano, M.P., M.D.V. and F. Pisanello. Data on in vivo use of tapered fibers are available from B.L.S.

Code availability
Custom code is available upon reasonable request to the corresponding authors. Custom code was used to: (i) extract the ring diameter from far-field measurements and report it in terms of k_t in the graph in Fig. 1g; (ii) extract the photometry efficiency field $\rho(x,y)$ from the collection $\xi(x,y)$ and the normalized illumination $\beta(x,y)$ fields; (iii) control the optical system to compare TF and FF collection in Fig. 3d,e; (iv) perform the in vivo experiments and elaborate the related dataset (Fig. 4 and Supplementary Fig. 6); (v) estimate light collection volumes from optical windows realized along the taper; (vi) to control the optical system to switch light emission and collection between W1 and W2 in Fig. 5m,n; (vii) 3D collection fields (Supplementary Figs. 1 and 7); (viii) perform the geometrical optics-based simulations of light collection with TFs reported in Supplementary Fig. 2; (ix) perform the quantitative estimation of the spatial distribution of the collected signal in Supplementary Fig. 3; (x) evaluate the contribution to integrated signal in Supplementary Fig. 4; (xi) control and extract data for the experiments on the evaluation of modal-mixing influence on the fluorescence signal collected by TFs (Supplementary Fig. 5).

References
37. Preibisch, S., Saalfeld, S. & Tomancak, P. Globally optimal stitching of tiled 3D microscopic image acquisitions. *Bioinformatics* **25**, 1463–1465 (2009).
38. Sileo, L., Pisanello, M., De Vittorio, M. & Pisanello, F. Fabrication of multipoint light emitting optical fibers for optogenetics. *Proc. SPIE* **9305**, 93052O (2015).

Corresponding author(s):   filippo.pisano@iit.it
massimo.devittorio@iit.it
bernardo_sabatini@hms.harvard.edu
ferruccio.pisanello@iit.it

Last updated by author(s): Jun 13,2019

Reporting Summary

Nature Research wishes to improve the reproducibility of the work that we publish. This form provides structure for consistency and transparency in reporting. For further information on Nature Research policies, see Authors & Referees and the Editorial Policy Checklist.

Statistics

For all statistical analyses, confirm that the following items are present in the figure legend, table legend, main text, or Methods section.

n/a	Confirmed	
☐	☒	The exact sample size (*n*) for each experimental group/condition, given as a discrete number and unit of measurement
☐	☒	A statement on whether measurements were taken from distinct samples or whether the same sample was measured repeatedly
☐	☒	The statistical test(s) used AND whether they are one- or two-sided *Only common tests should be described solely by name; describe more complex techniques in the Methods section.*
☒	☐	A description of all covariates tested
☐	☒	A description of any assumptions or corrections, such as tests of normality and adjustment for multiple comparisons
☐	☒	A full description of the statistical parameters including central tendency (e.g. means) or other basic estimates (e.g. regression coefficient) AND variation (e.g. standard deviation) or associated estimates of uncertainty (e.g. confidence intervals)
☐	☒	For null hypothesis testing, the test statistic (e.g. *F*, *t*, *r*) with confidence intervals, effect sizes, degrees of freedom and *P* value noted *Give P values as exact values whenever suitable.*
☒	☐	For Bayesian analysis, information on the choice of priors and Markov chain Monte Carlo settings
☒	☐	For hierarchical and complex designs, identification of the appropriate level for tests and full reporting of outcomes
☐	☒	Estimates of effect sizes (e.g. Cohen's *d*, Pearson's *r*), indicating how they were calculated

Our web collection on statistics for biologists contains articles on many of the points above.

Software and code

Policy information about availability of computer code

Data collection	Vidrio ScanImage Premium ; NI Labview 2017; Matlab R2016b
Data analysis	Matlab R2016b, FIJI, G*Power 3.1.9.2

For manuscripts utilizing custom algorithms or software that are central to the research but not yet described in published literature, software must be made available to editors/reviewers. We strongly encourage code deposition in a community repository (e.g. GitHub). See the Nature Research guidelines for submitting code & software for further information.

Data

Policy information about availability of data

All manuscripts must include a data availability statement. This statement should provide the following information, where applicable:

- Accession codes, unique identifiers, or web links for publicly available datasets
- A list of figures that have associated raw data
- A description of any restrictions on data availability

Data are available upon reasonable request.

Field-specific reporting

Please select the one below that is the best fit for your research. If you are not sure, read the appropriate sections before making your selection.

☒ Life sciences   ☐ Behavioural & social sciences   ☐ Ecological, evolutionary & environmental sciences

Life sciences study design

All studies must disclose on these points even when the disclosure is negative.

Sample size	Fluorimetry data: sample size was estimated based on Cohen's d parameter using G*Power software.
Data exclusions	For in-vivo fiber photometry experiments, mice without signals were excluded from the analysis. For all other experiments, no data has been excluded.
Replication	In fluorimetry measurements, technical replication was performed by repeating every measurement 3 times; biological replication was tested across uncorrelated brain slices, uncorrelated insertion positions and in two brain areas: cortex and striatum. In light collection field measurements, technical replication has been performed by measuring every field over 60 acquisitions, with excitation powers well below the photobleaching condition; biological replication has been verified by inserting fibers in various positions in different tissue samples from mouse brain. All attempts of replications were successfull. For in-vivo fiber photometry experiments, photometry signals were collected from 4 mice (2 sessions/mouse) and analyzed; the measurements showed similar trends across all 4 mice.
Randomization	Brain slices samples were chosen randomly. Tapered and flat fibers were fabricated in batches and selected for uniformity based on visual inspection at the optical microscope.
Blinding	Blinding was used between fibers belonging to the same group, with groups being defined as: "Tapered fibers with a specific taper angle, core diameter and numerical aperture" and "Flat fibers with specific core diameter and numerical aperture".

Reporting for specific materials, systems and methods

We require information from authors about some types of materials, experimental systems and methods used in many studies. Here, indicate whether each material, system or method listed is relevant to your study. If you are not sure if a list item applies to your research, read the appropriate section before selecting a response.

Materials & experimental systems

n/a	Involved in the study
☒	Antibodies
☒	Eukaryotic cell lines
☒	Palaeontology
☐	☒ Animals and other organisms
☒	Human research participants
☒	Clinical data

Methods

n/a	Involved in the study
☒	ChIP-seq
☒	Flow cytometry
☒	MRI-based neuroimaging

Animals and other organisms

Policy information about studies involving animals; ARRIVE guidelines recommended for reporting animal research

Laboratory animals	mouse, both sexes, Thy1:ChR2:eYFP; male C57BL/6J, 9 weeks old
Wild animals	None
Field-collected samples	None
Ethics oversight	Harvard Medical Area Standing Committee on Animals

Note that full information on the approval of the study protocol must also be provided in the manuscript.